Arctic black shale formation during Cretaceous Oceanic Anoxic Event 2

M. Lenniger, H. Nøhr-Hansen, L. V. Hills and C. J. Bjerrum

SUPPLEMENTARY MATERIAL

Sample location

The investigated May Point succession is located on easternmost Axel Heiberg Island, Canada (79° 19' 39" N 85° 32' 27" W).

Methods

Between 100 to 150 g of sample material were collected from fresh solid rock outcrops in cliffs and river cutbanks (Nunez-Betelu, 1994). Scree-covered outcrops were excavated for about 20-30 cm into the outcrop until permafrost was reached, for fresh and clean solid samples. Collected sample material was sealed in plastic bags, shipped via air cargo and directly air dried in the opened bags once the samples arrived at the University of Calgary.

Splits of outcrop samples were powdered using an agate mortar. For isotope measurements of bulk organic matter (OM) 0.9 g of each sample were decarbonised. For this, samples were treated twice with 15 ml of 1M HCL and left in a shaker for in total 36 h to remove carbonate carbon. The residue was centrifuged, rinsed with deionized water and centrifuged again, repeating the process until the pH of deionized water was reached. The samples were then freeze dried for at least 48h. Total organic carbon (TOC) and total sulfur content (TS) of the decarbonised material was measured on an Eltra CS500 elemental analyser. Long-term reproducibility of the instrument is better than ± 0.2% for TOC and 0.3% for TS. Depending on the TOC content of the sample, between 3 to 75 mg of sample powder were wrapped in tin foil cups, so that 0.06 mg of carbon was combusted in a EuroVector Euro EA 3000 elemental analyser connected to an Isoprime dual-inlet stable isotope ratio mass spectrometer. Every tenth sample was run in duplicate and internal standards were interspersed throughout the batch of samples. Samples were point calibrated toward a calibration curve made of 10 different weights of the internal laboratory standard, thus bracketing the pure carbon weights of the samples. Measured carbon isotope ratios were corrected against the calibrated (USGS-24) internal standard AK (reproducibility better than ±0.06‰) and reported in standard δ–notation in per mil (‰) relative to the international VPDB isotope standard.

For trace and minor element analyses about 0.1 g of sample powder were digested in a mixture of 1 ml 65% nitric acid and 5 ml 40% hydrofluoric acid and placed in a closed Savillex vessel (polytetrafluorethylene polymer) on a hotplate at 130°C for 24h. Samples

were then dried in the vessel on the hotplate, treated with 1 ml 65% nitric acid and evaporated to dryness again. This process was repeated, then 2.5 ml 65% nitric acid and Milli-Q was added and the closed vessel was placed on the hotplate at 130°C. After at least 12 h on the hotplate the sample was diluted with Milli-Q to 50 ml. Prior to the analyses this solution was further diluted (11 times) and measured using a PerkinElmer Elan 6100DRC ICP-MS at the Geological Survey of Denmark and Greenland. Measurements of the certified USGS standard BHVO-2 yielded accuracies (Al <0.1%, Fe <0.8%, Ti <2.4%, Mo <7.8%, Y <3.0% and Zr <0.8%) that are within the accepted analytical error.

TABLE DR1. HH-XRF PERFORMANCE

Element	Certified values (PACS-2)	Raw mean (n=24)	Precision (σ) (n=24)	Relative standard deviation (%)	Corrected mean
Al	6.62 ±0.32 wt%	4.20 wt%	0.08 wt%	1.9	5.03 ±1.06 wt%
Fe	4.09 ±0.06 wt%	4.95 wt%	0.05 wt%	1.0	4.08 ±0.76 wt%
Ti	0.44 ±0.03 wt%	0.43 wt%	0.01 wt%	2.1	0.43 ±0.01 wt%
Y	14.1 ±0.44 ppm*	15 ppm	<1 ppm	4.4	16 ±1 ppm
Zr	-	127 ppm	12 ppm	9.2	112 ±22 ppm
Mo	5.43 ±0.28 ppm	7 ppm	<1 ppm	9.5	7 ±2 ppm

*recommended value (Shaheen and Fryer, 2011)

Additional trace (Mo, Y and Zr) and minor element (Al, Ti and Fe_T) analyses were performed using an Olympus DP-6000 handheld XRF (HH-XRF) analyser with a Rh tube (for a detailed description see Dahl et al., 2013). A certified international reference material (PACS-2) was measured along with the samples to assure the reproducibility of the analyses (see Table DR1). The relative standard deviation (%RSD) for all the analysed elements is typically smaller than 10% for trace elements and smaller than 2% for minor elements. HH-XRF raw data were corrected by reduced major axis regression against the results from the ICP-MS analyses measured on splits of the powdered samples (Fig. DR1). The majority of the calibration curves have R^2 >0.88 between samples measured by ICP-MS and the corresponding HH-XRF measurements (Table DR2). However, the calibration curve for aluminium is more variable and displays various data points that deviate from the calibration line. These larger variations are probably related to interferences between the energy peaks of aluminium and silicon that can occur in both ICP-MS and XRF analyses and is reflected in a relative high standard error (σ) for aluminium. The corrected data of PACS-2 typically fall within the range of the reported certified values and confirm that a combination of HH-XRF and ICP-MS analyses can provide a reliable dataset for paleoenvironment studies (Dahl et al., 2013).

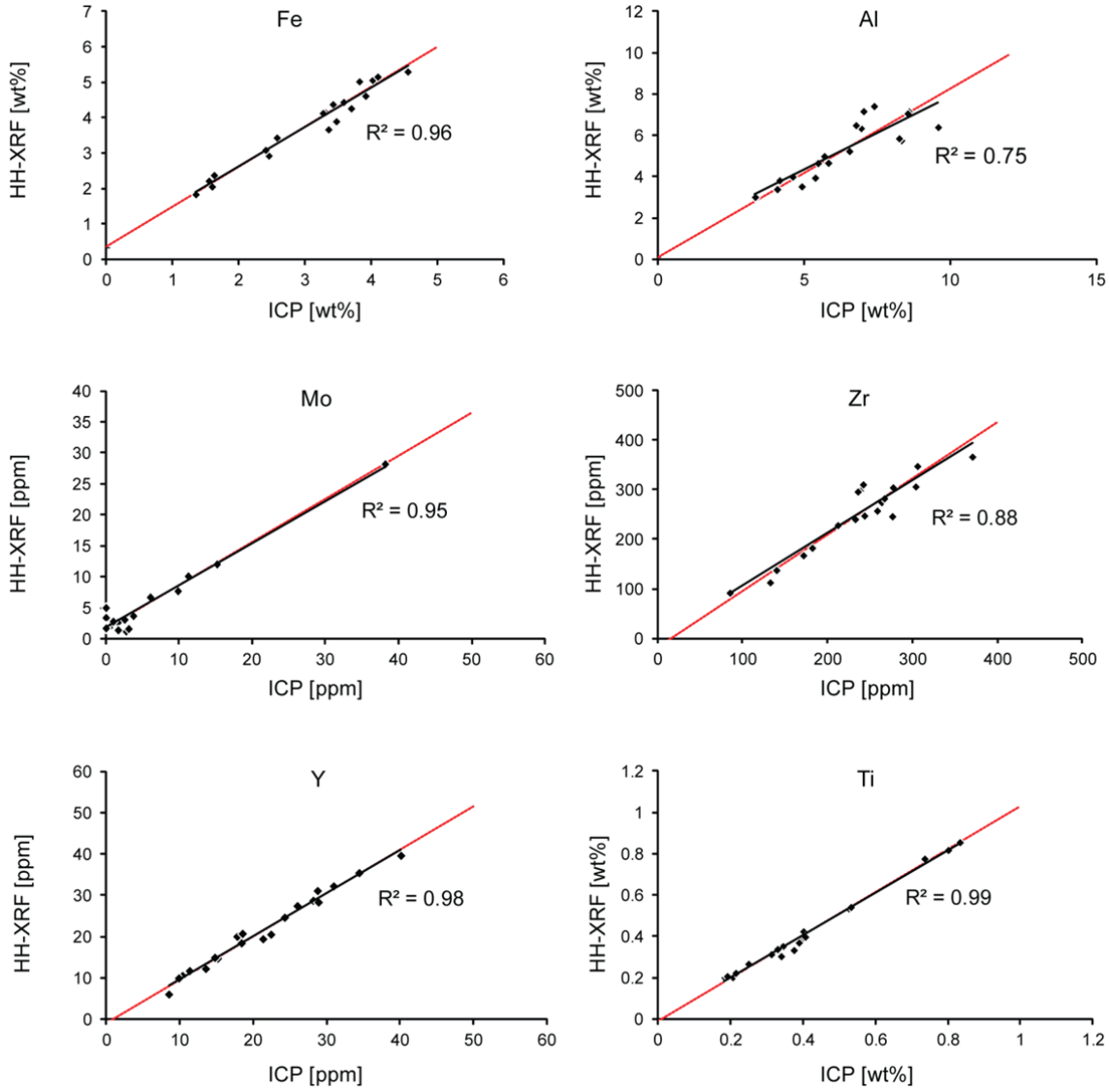

Figure DR1: Crossplots of HH-XRF raw data vs. ICP-MS data. The black line represents the linear regression and the red line the reduced major axis regression. For details see Table DR2.

Iron speciation and pyrite sulfur isotope ratios were measured at the Institute of Biology, University of Southern Denmark. Sulfur isotope ratios are reported in standard δ–notation in per mil (‰) relative to the Vienna Canyon Diablo Troilite (CDT). Repeated analyses of IAEA-S-1 show a reproducibility of better than ±0.2‰ for sulfur isotope ratios. A detailed description of the methodologies used can be found in Hammarlund et al. (2012) and Poulton and Canfield (2005).

TABLE DR2. ICP vs. HH-XRF

Element	Reduced major axis regression				
	Slope (a)	Intercept (b)	Coefficient of determination (R^2)	Standard error (95% CI)	Number of measurements
Al	0.81	0.10	0.75	1.06 wt%	19 (1 outlier)
Fe	1.13	0.34	0.96	0.76 wt%	20
Ti	1.04	-0.01	0.99	0.01 wt%	19 (1 outlier)
Y	1.05	-1.00	0.98	<1 ppm	20
Zr	1.13	-16.88	0.88	22 ppm	19 (1 outlier)
Mo	0.70	1.74	0.95	2 ppm	18 (1 outlier)

Hydrogen index values (HI) from Rock-Eval pyrolysis are from Nunez-Betelu (1993, 1994) under supervision of L. V. Hills . These HI analyses were carried out on a Delsi II Rock-Eval/TOC pyrolysis unit equipped with a total organic carbon (TOC) analysis module. Samples were run in duplicate and an internal standard was measured every fifteenth sample. Randomly selected samples were re-run to ensure consistency. The hydrogen index is defined as (S_2/TOC)*100= HI [mgHC/g TOC], where S_2 represents the amount of pyrolyzed hydrocarbons. Repeated analyses of the internal standard yield a reproducibility of better than ±0.52 mg HC/g sample for S_2 and 0.18% for TOC.

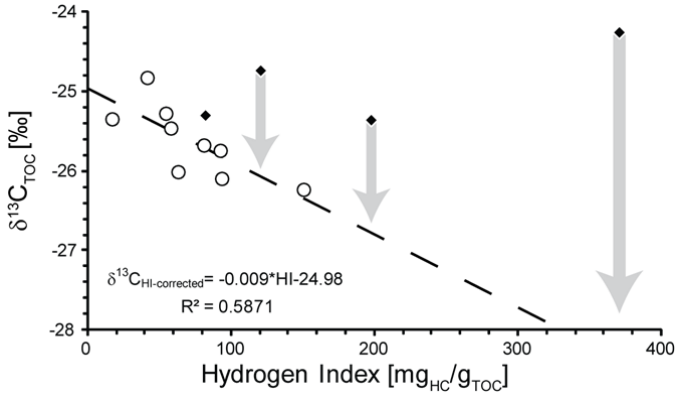

Figure DR2. Crossplot of $\delta^{13}C_{TOC}$ (this study) vs. hydrogen index values (from Nunez-Betelu, 1994). Late Turonian to Coniacian samples (circles) display a moderate negative correlation for $\delta^{13}C_{TOC}$ and HI values, caused by organic matter sourcing. However, CTB samples (black diamonds) do not follow the negative correlation indicating that the $\delta^{13}C_{TOC}$ signal of these samples is governed by changes other than organic matter sourcing. Subtracting the $\delta^{13}C$ values calculated as a function of organic matter sourcing from the $\delta^{13}C_{TOC}$ data effects ($\Delta^{13}C_{HI\ corrected} = \delta^{13}C_{TOC} - \delta^{13}C_{HI\text{-}corrected}$) results in a carbon isotope signal that resembles changes in the global carbon cycle without being altered by organic matter sourcing (van de Schootbrugge et al., 2013). Note that HI values are not available for all the isotope data so that missing values have been derived by linear interpolation between adjacent data points.

However, the crossplot and the analytical definition for $\delta^{13}C_{HI\text{-}corrected}$ is based only on actually measured HI values (from Nunez-Betelu, 1994) .

Mass accumulation rates of total organic carbon (MARTOC)

The bio- and chemostratigraphic correlation between May Point, Pueblo and the reference profile from the English chalk (Fig. 1) allows calculation of linear sedimentation rates between the different correlated isotopic events (Fig DR3 and Table DR3). The calculations assume that sedimentation rates between two correlation points are constant and that no major hiatuses occurred.

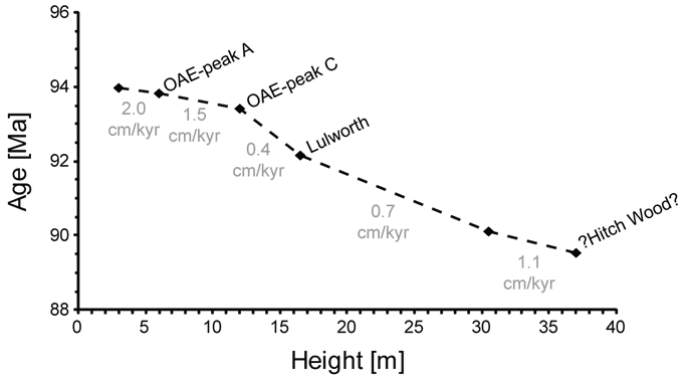

Figure DR3. Age model for the May Point succession on Axel Heiberg Island (Canada). Identification of isotope events is based on bio- and chemostratigraphic correlation (Figure 1). Assigned ages are derived from the age calibrated English carbon –isotope reference curve (Jarvis et al., 2006).

For calculation of sediment accumulation rates (SAR) we assume a constant rock density of 2.6 g/cm^3.

SAR [g/cm^2/kyr] = sedimentation rate [cm/kyr] x rock density [g/cm^3]

Bulk rock total organic carbon concentrations were converted into mass accumulation rates of total organic carbon (MARTOC) as follows.

MARTOC [g/cm2/kyr] = SAR [g/cm2/kyr] x TOC [%]/100

Bulk sediment accumulation rates (SAR) are high prior to OAE2 and decrease to a minimum just after the event, before they slowly increase again up section. Based on these observations we place a maximum flooding surface after OAE2 and suggest that the lower part of the Bituminous Member , Kanguk Formation, was deposited during a transgression. This interpretation is in accordance with the presented Ti/Al ratios (Fig. DR4) and previous

studies from the nearby Glacier Fiord section (Nunez-Betelu, 1994; Schröder-Adams et al., 2014).

TABLE DR3. AGE MODEL

Sample number	Height (m)	Age marker (Ma)	Isotope event	Sedimentation rate (cm/kyr)	Sediment accumulation rate (g/cm^2/kyr)
MP-06	3.0	94.0	-	2.0	5.3
MP-08	6.0	93.8	OAE-peak A	1.5	3.8
MP-12	12.0	93.4	OAE-peak C	0.4	0.9
MP-15	16.5	92.2	Lulworth	0.7	1.8
MP-27	30.5	90.1	-	1.1	2.9
MP-31	37.0	89.6	?Hitch wood?	1.1	2.9

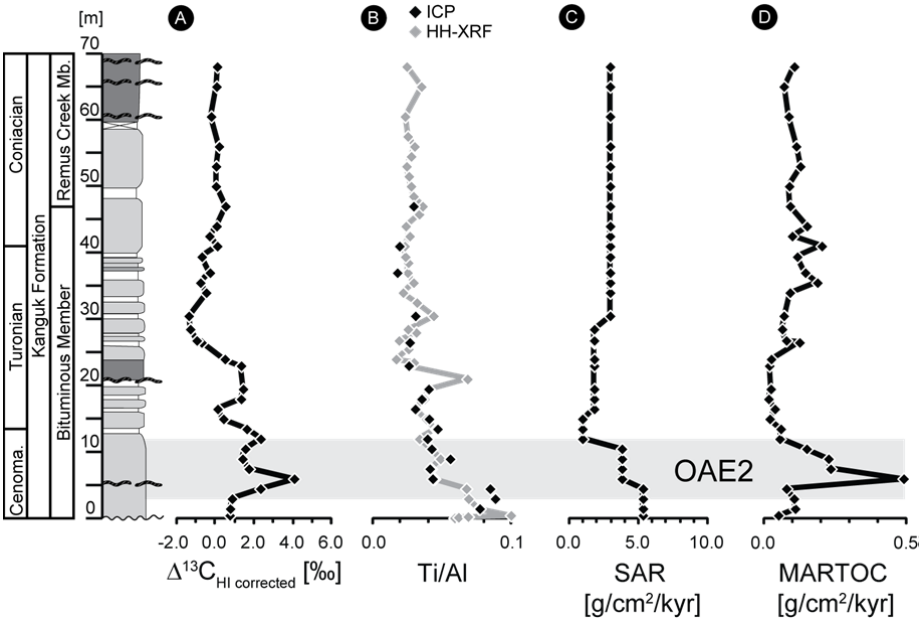

Figure DR4. Carbon isotope stratigraphy and mass accumulation rates from the May Point succession on Axel Heiberg Island (Canada). A) Carbon isotope stratigraphy ($\Delta^{13}C_{HI\ corrected}$). B) Bulk sediment Ti/Al-ratios. ICP data (black) and corrected HH-XRF data (gray). C) Sediment accumulation rates (SAR). D) Mass accumulation rates of total organic carbon (MARTOC). Legend as in Figure 1.

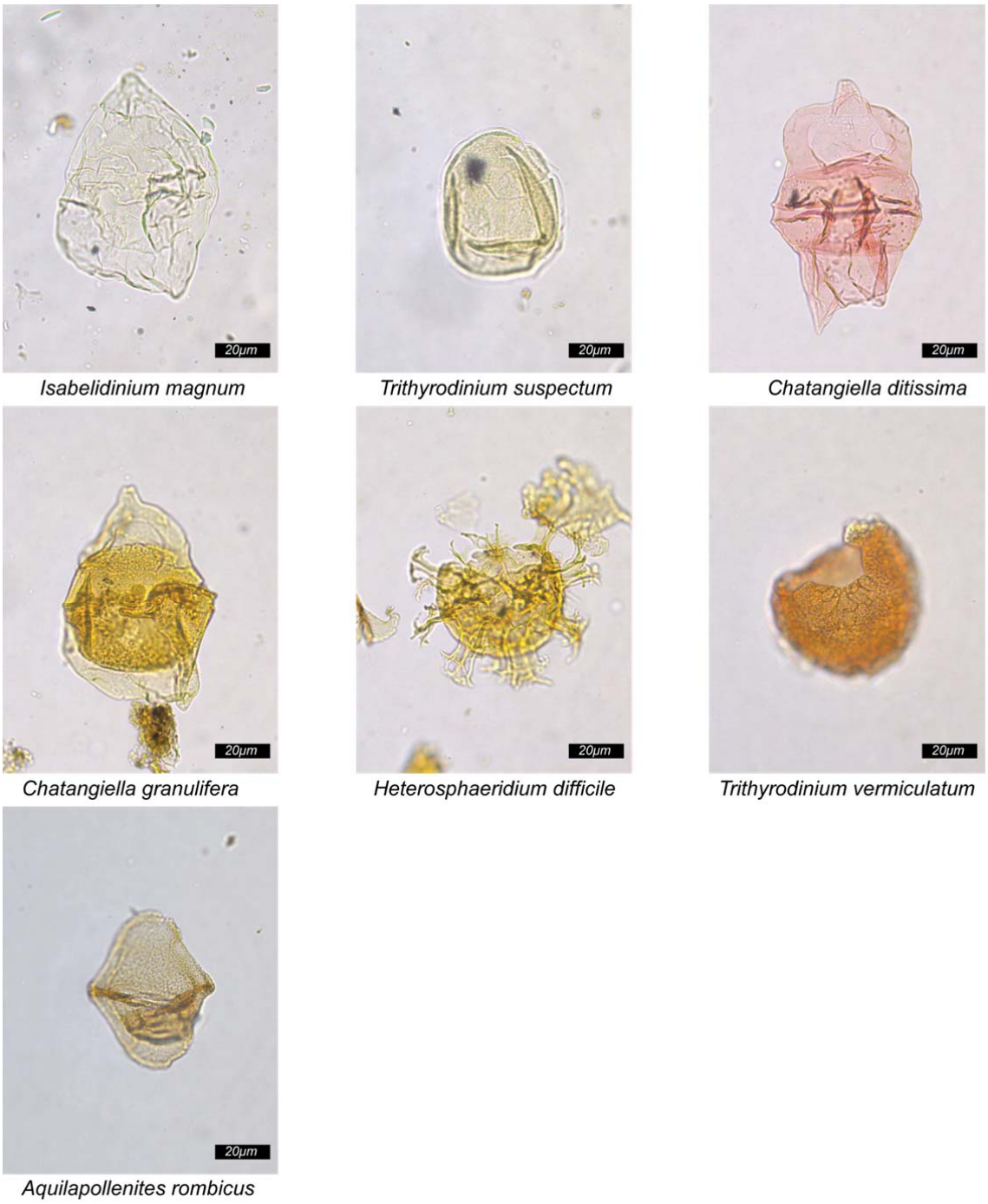

Figure DR5. Transmitted Light microscope images of selected key biostratigraphic species.

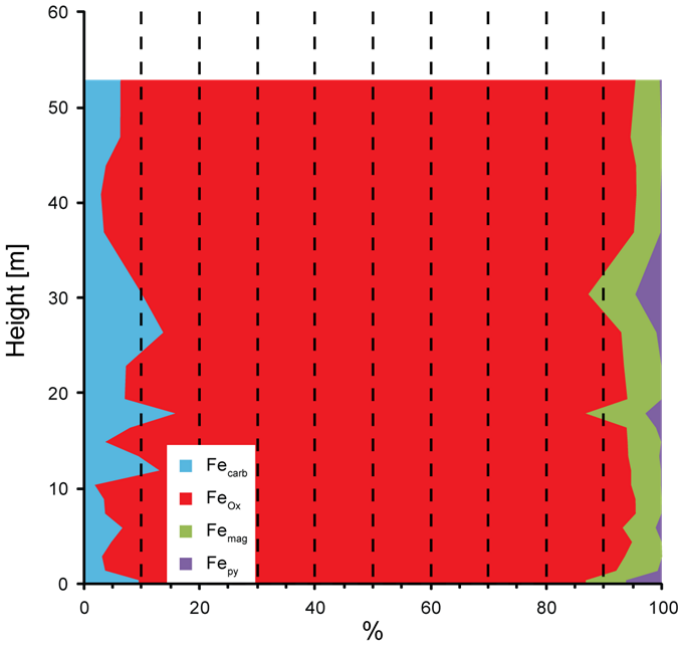

Figure DR6. Relative composition of the total Fe_{HR} iron pool shown across the succession.

Discriminating volcanic influence on the Fe-speciation proxy

Sediments of the Kanguk Formation are interbedded with up to metre thick bentonites that formed from distal volcanic ash fallout from a peralkaline rhyolitic magma source (Parsons, 1994; Patchett et al., 2004). Patchett et al. (2004) measured Nd isotopes on various sediment and two bentonite samples from the Kanguk Formation. Patchett et al. concluded that Late Turonian to Santonian mudstones of the Kanguk Formation are to an uncertain degree mixed with volcanogenic material. The major Fe-bearing phase in the Kanguk bentonites is ilmenite (Parsons, 1994). However, prior to burial the volcanic ash may have also contained other more reactive Fe-bearing phases that formed during atmospheric processing (e.g. hematite or Fe oxyhydroxides) (Ayris and Delmelle, 2012 and references therein). Potentially mixing between two sources of detrital and volcanogenic iron may have affected iron speciation characteristics and make reliable paleoredox reconstructions from Fe speciation data difficult.

Ratios of the immobile elements Ti, Zr, and Y are used to identify mudstone samples that show potential mixing with volcanogenic material (Winchester and Floyd, 1977). Similar element-ratios (e.g. TiO_2/Al_2O_3 vs. Zr/Al_2O_3) have previously been used to distinguish detrital from volcanogenic clay-rich beds in the English chalk (Wray and Wood, 1998). A crossplot of Zr/Ti vs. Y/Ti allows identification of potential mixing between the sediments and the felsic volcanic ash/bentonites (Fig. DR7). The crossplot shows that sediments and bentonites plot in two distinct fields, where bentonites are characterised by variable high Zr/Ti and Y/Ti ratios. Mudstone samples generally show significantly lower element ratios comparable to compositions of average shale or upper continental crust (Taylor and McLennan, 1995; Wedepohl, 1971). A few mudstone samples display elevated Zr/Ti and

Y/Ti ratios, indicating some degree of in-mixed volcanogenic material. These “ash contaminated” mudstone samples are usually situated directly in contact with the identified bentonites (Fig. DR8). Mudstones deposited during OAE2 show consistently low element ratios, indicating at the most minor volcanogenic contamination and that iron speciation characteristics of sediments deposited during OAE2 are controlled by paleoredox conditions.

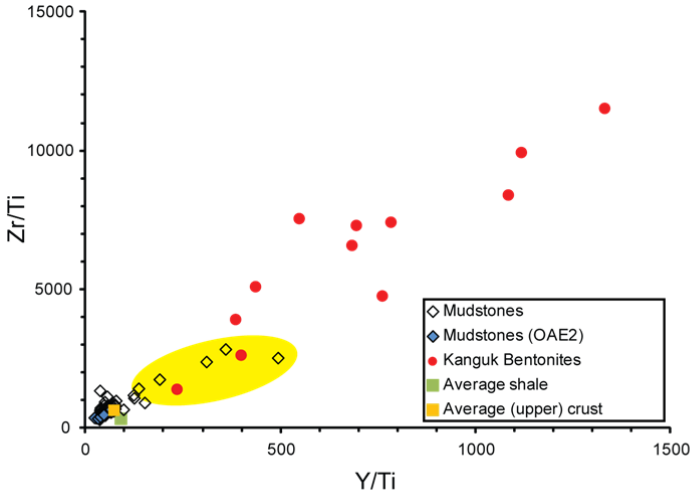

Figure DR7: Crossplot of Zr/Ti vs. Y/Ti (corrected HH-XRF data). Mudstone samples (this study), average shale after Wedepohl (1971), various Kanguk bentonites from Parsons (1994) and average upper continental crust after Taylor and McLennan (1995). Yellow ellipse indicates samples that show potential mixing between sediment and volcanic material.

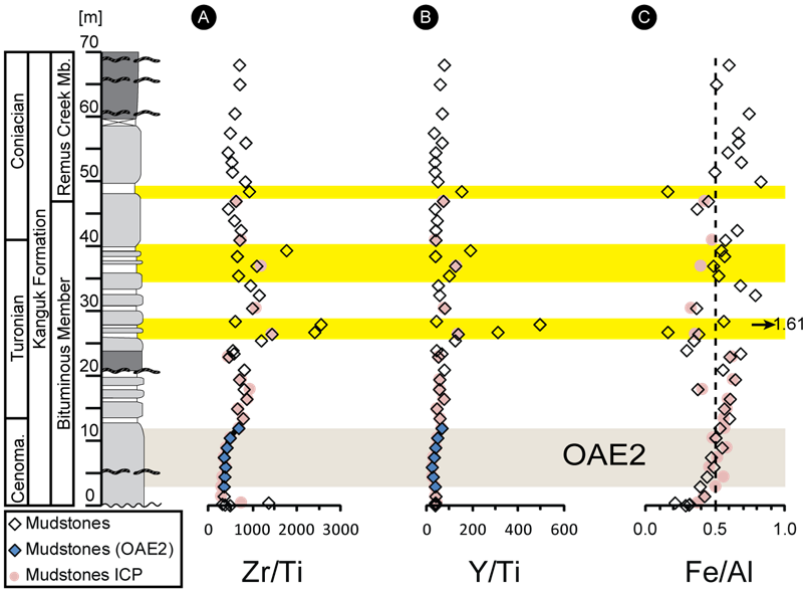

Figure DR8: Trace element records from the May Point succession on Axel Heiberg Island (Canada). A) Bulk rock Zr/Ti-ratios. B) Bulk rock Y/Ti-ratios. C) Bulk rock Fe/Al-ratios. Dashed line represents the commonly used detrital background value of normal marine (oxic)

sediments derived from Fe/Al-ratios in average shale (Raiswell and Canfield, 2012; Wedepohl, 1971). Corrected HH-XRF data (diamonds) and ICP data (red circles). The yellow bars indicate horizons of potential mixing between sediment and volcanic material as diagnosed in Figure DR7. For legend see Figure DR7.

Bottom water restriction and reservoir effects

During OAE2 we observe high TOC values along with strikingly low Mo and Mo/TOC values, similar to previously described Mo perturbations from Demerara Rise (Hetzel et al., 2009) (Table DR4). Hetzel et al. (2009) suggested that the subdued Mo signal was related to a regional or even more widespread drawdown of the seawater Mo inventory caused by the expansion of anoxic depositional environments during the onset of OAE2 (Hetzel et al., 2009). The low Mo of the black shales in the Sverdrup Basin suggests a similar scenario. Despite low average Mo/TOC values (Table DR4), indicating strong hydrographic bottom water restriction (Algeo and Lyons, 2006), fluctuations in Mo after OAE2 usually coincide with similar changes in TOC ($r=0.6$), suggesting that Mo enrichments are instead controlled by H_2S availability as opposed to limited seawater Mo concentrations caused by bottom water restriction (Owens et al., 2012).

TABLE DR4. DATA MAY POINT/CANADA

Sample number	Height (m)	Total organic carbon (wt%)	Total sulfur (wt%)	Corrected HH-XRF data						Mo/TOC	$\delta^{13}C_{TOC}$ (‰)	$\Delta^{13}C$ (‰)
				Ti (wt%)	Al (wt%)	Fe (wt%)	Zr (ppm)	Y (ppm)	Mo (ppm)			
MP-1	0.1	-	-	0.87	10.97	3.10	418	31	4	-	-	-
MP-2	0.2	-	-	0.81	9.97	3.05	300	29	1	-	-	-
MP-3	0.3	-	-	0.86	9.69	3.02	265	30	1	-	-	-
MP-4	0.5	0.9	0.2	0.96	8.01	1.66	1298	35	15	15.8	-24.58	0.74
MP-5	1.5	2.0	0.1	0.83	8.67	3.62	289	32	3	1.4	-24.64	0.76
MP-6	3.0	2.0	0.0	0.80	8.98	3.47	278	28	1	0.3	-24.58	0.86
MP-7	4.5	1.5	0.1	0.76	8.68	3.78	276	20	2	1.6	-24.56	2.32
MP-8	6.0	12.9	1.0	0.30	4.72	2.29	115	7	N.D.*	-	-24.25	4.05
MP-9	7.5	6.1	0.5	0.39	6.30	2.94	137	12	N.D.*	-	-25.81	1.72
MP-10	9.0	5.9	0.4	0.53	7.67	4.17	217	19	N.D.*	-	-25.35	1.40
MP-11	10.5	3.9	0.6	0.53	8.54	4.26	258	24	1	0.3	-25.29	1.54
MP-12	12.0	5.8	0.4	0.42	7.84	4.14	284	27	2	0.3	-24.58	2.33
MP-13	13.5	6.2	0.4	0.37	5.61	3.35	285	20	5	0.8	-25.04	1.61
MP-14	15.0	2.1	0.1	0.35	6.00	3.36	228	15	N.D.*	-	-25.29	0.42
MP-15	16.5	2.1	0.1	0.20	4.04	2.43	176	15	N.D.*	-	-25.77	0.12
MP-16	18.0	0.9	0.0	0.20	3.58	1.32	163	11	2	1.8	-24.73	1.33
MP-17	19.5	1.3	0.1	0.34	5.59	3.57	234	18	12	9.3	-24.47	1.43
MP-18	21.0	-	-	0.42	4.77	2.62	338	31	4	-	-24.52	1.33
MP-19	23.0	1.0	0.1	0.21	4.57	2.74	96	10	N.D.*	-	-	-
MP-20	23.5	-	-	0.27	5.36	3.63	151	17	2	-	-	-
MP-21	24.0	1.4	0.1	0.20	5.58	1.62	111	8	N.D.*	-	-25.41	0.49
MP-22	25.5	-	-	0.22	4.79	1.64	260	27	4	-	-	-
MP-23	26.5	6.9	0.5	0.23	4.79	1.80	322	30	15	2.1	-26.68	-0.71
MP-24	26.8	4.3	0.5	0.17	4.42	0.69	408	53	13	3.0	-26.93	-0.96
MP-25	28.0	-	-	0.13	2.53	4.09	328	64	5	-	-	-
MP-26	28.5	3.5	0.3	0.22	4.97	2.76	134	9	N.D.*	-	-27.24	-1.29
MP-27	30.5	2.3	0.3	0.27	4.20	1.52	264	21	7	3.0	-27.10	-1.37
MP-28	32.5	-	-	0.21	4.15	3.25	245	12	2	-	-	-
MP-29	34.0	3.1	0.6	0.29	6.96	4.70	274	14	5	1.6	-26.01	-0.47
MP-30	35.5	6.3	0.5	0.34	6.90	3.59	228	33	10	1.6	-26.44	-0.77
MP-31	37.0	4.9	0.5	0.31	6.95	3.35	339	39	9	1.7	-26.09	-0.28
MP-32	38.5	-	-	0.37	8.06	4.52	236	13	6	-	-	-
MP-33	39.4	3.9	0.5	0.29	6.63	3.57	505	54	17	4.4	-26.82	-0.70
MP-34	41.0	6.9	1.0	0.33	7.73	4.39	232	13	38	5.5	-26.23	0.10
MP-35	42.5	3.3	0.4	0.26	5.58	3.64	189	10	3	0.9	-26.37	-0.30
MP-36	44.0	5.1	1.1	0.28	6.38	6.51	162	12	11	2.1	-25.74	0.07
MP-37	45.8	-	-	0.33	6.26	2.28	148	12	N.D.*	-	-	-
MP-38	47.0	3.1	0.3	0.39	7.06	3.14	242	28	3	0.9	-24.82	0.52
MP-39	48.5	-	-	0.30	6.18	0.95	279	46	6	-	-	-
MP-40	50.0	3.0	0.3	0.26	5.42	4.45	212	12	3	1.0	-25.67	0.03
MP-41	51.5	-	-	0.37	8.16	4.01	201	13	2	-	-	-

MP-42	53.0	4.3	0.8	0.35	7.93	5.40	183	12	4	1.0	-25.46	0.04
MP-43	54.5	-	-	0.36	7.66	4.48	159	14	N.D.*	-	-	-
MP-44	56.0	3.8	0.5	0.34	6.73	4.45	282	22	6	1.5	-25.27	0.19
MP-45	57.5	-	-	0.38	8.40	5.55	184	12	2	-	-	-
MP-46	60.5	2.9	0.2	0.34	8.00	5.89	204	23	1	0.3	-25.34	-0.22
MP-47	65.0	2.3	0.1	0.47	8.56	4.30	330	27	4	1.6	-25.11	0.06
MP-48	68.0	3.6	0.1	0.43	9.61	5.70	296	32	4	1.1	-25.09	0.09

* Measured concentrations below the HH-XRF detection limit (N.D.) are in figures substituted with a constant value of zero.

TABLE DR5. IRON SPECIATION AND SULFUR ISOTOPE DATA

Sample number	Height (m)	Fe_T (wt%)	Fe_{carb} (wt%)	Fe_{Ox} (wt%)	Fe_{mag} (wt%)	Fe_{Py} (wt%)	FeHR (wt%)	Fe_{HR}/Fe_T	Fe_{Py}/Fe_{HR}	Theoretical Fe_{py} calculations based on total sulfur		$\delta^{34}S_{Py}$ (‰)
										$Fe_{Py\ calc}$ (wt%)	$Fe_{Py\ calc}/Fe_{HR}$	
MP-4	0.5	1.55	0.08	0.68	0.06	0.06	0.88	0.57	0.06	0.15	0.17	-28.42
MP-5	1.5	3.58	0.08	2.04	0.17	0.02	2.31	0.64	0.01	0.06	0.02	8.34
MP-6	3.0	3.70	0.07	2.13	0.15	0.00	2.36	0.64	0.00	0.04	0.02	3.35
MP-7	4.5	3.91	0.11	2.22	0.13	0.01	2.47	0.63	0.00	0.10	0.04	13.64
MP-8	6.0	2.45	0.09	1.27	0.08	0.02	1.46	0.60	0.01	0.86	0.59	-10.38
MP-9	7.5	3.35	0.08	2.00	0.10	0.01	2.18	0.65	0.00	0.41	0.19	-12.56
MP-10	9.0	4.02	0.09	2.46	0.12	0.01	2.68	0.67	0.00	0.38	0.14	-10.60
MP-11	10.5	4.10	0.04	2.15	0.12	0.01	2.31	0.56	0.00	0.51	0.22	-17.85
MP-12	12.0	3.82	0.27	1.69	0.11	0.01	2.07	0.54	0.00	0.37	0.18	-14.24
MP-13	13.5	3.25	0.20	1.83	0.12	0.01	2.16	0.66	0.01	0.34	0.16	-16.42
MP-14	15.0	3.30	0.07	1.87	0.12	0.01	2.07	0.63	0.00	0.12	0.06	-18.90
MP-15	16.5	2.40	0.12	1.33	0.08	0.02	1.55	0.65	0.01	0.11	0.07	-22.31
MP-16	18.0	1.35	0.07	0.33	0.05	0.01	0.46	0.34	0.03	-	-	-16.27
MP-17	19.5	3.42	0.12	1.57	0.11	0.01	1.81	0.53	0.00	0.10	0.05	-
MP-19	23.0	2.57	0.09	1.13	0.09	0.00	1.31	0.51	0.00	0.09	0.07	-
MP-23	26.5	1.62	0.13	0.75	0.06	0.01	0.95	0.58	0.01	0.44	0.46	-19.03
MP-27	30.5	1.59	0.06	0.49	0.05	0.03	0.64	0.40	0.05	0.23	0.36	-31.98
MP-30	-	-	-	-	-	-	-	-	-	-	-	-22.36
MP-31	37.0	3.27	0.07	2.03	0.10	0.01	2.22	0.68	0.00	0.42	0.19	-21.41
MP-34	41.0	4.55	0.09	2.91	0.13	0.01	3.14	0.69	0.00	0.83	0.27	-21.99
MP-36	44.0	-	0.22	5.51	0.27	0.01	6.00	-	0.00	0.94	0.16	-30.35
MP-38	47.0	3.47	0.12	1.71	0.10	0.01	1.94	0.56	0.00	0.24	0.12	-26.84
MP-42	53	-	0.22	3.22	0.15	0.02	3.62	-	0.01	0.70	0.19	-24.82

TABLE DR6. ICP DATA

Sample number	Height (m)	Ti (wt%)	Al (wt%)	Fe (wt%)	Zr (ppm)	Y (ppm)	Mo (ppm)
MP-4	0.5	0.79	4.16	1.55	585.64	34.46	N.D.*
MP-5	1.5	0.83	8.58	3.58	241.80	31.00	N.D.*
MP-6	3.0	0.80	7.40	3.70	238.10	28.21	0.70
MP-7	4.5	0.74	7.04	3.91	235.60	17.85	N.D.*
MP-8	6.0	0.34	5.38	2.45	132.39	8.56	5.74
MP-9	7.5	0.40	6.55	3.35	139.79	11.39	2.74
MP-10	9.0	0.53	6.95	4.02	212.05	21.38	N.D.*
MP-11	10.5	0.53	8.55	4.10	263.46	24.33	1.62
MP-12	12.0	0.40	6.78	3.82	277.00	26.06	2.54
MP-13	13.5	0.39	5.83	3.25	303.70	22.48	N.D.*
MP-14	15.0	0.34	5.69	3.30	232.45	15.20	1.66
MP-15	16.5	0.21	4.08	2.40	181.88	14.81	3.10
MP-16	18.0	0.18	3.33	1.35	171.47	10.40	0.99
MP-17	19.5	0.33	5.48	3.42	243.36	18.45	11.23
MP-19	23.0	0.19	4.17	2.57	84.99	9.91	N.D.*
MP-23	26.5	0.21	4.61	1.62	305.75	28.80	15.17
MP-27	30.5	0.25	4.92	1.59	266.70	18.59	6.06
MP-31	37.0	0.31	8.33	3.27	370.37	40.16	9.83
MP-34	41.0	0.37	9.59	4.55	276.16	13.58	38.13
MP-38	47	0.41	8.25	3.47	258.36	28.93	3.74

* In figures substituted with a constant value of zero.

References

Algeo, T.J., and Lyons, T.W., 2006, Mo-total organic carbon covariation in modern anoxic marine environments: Implications for analysis of paleoredox and paleohydrographic conditions: Paleoceanography, v. 21, Pa1016, doi:10.1029/2004pa001112.

Ayris, P., and Delmelle, P., 2012, Volcanic and atmospheric controls on ash iron solubility: A review: Physics and Chemistry of the Earth, Parts A/B/C, v. 45–46, p. 103–112.

Dahl, T.W., Ruhl, M., Hammarlund, E.U., Canfield, D.E., Rosing, M.T., and Bjerrum, C.J., 2013, Tracing euxinia by molybdenum concentrations in sediments using handheld X-ray fluorescence spectroscopy (HHXRF): Chemical Geology, v. 360, p. 241–251.

Hammarlund, E.U., Dahl, T.W., Harper, D.A.T., Bond, D.P.G., Nielsen, A.T., Bjerrum, C.J., Schovsbo, N.H., Schonlaub, H.P., Zalasiewicz, J.A., and Canfield, D.E., 2012, A sulfidic driver for the end-Ordovician mass extinction: Earth and Planetary Science Letters, v. 331, p. 128–139.

Hetzel, A., Bottcher, M.E., Wortmann, U.G., and Brumsack, H.J., 2009, Paleo-redox conditions during OAE 2 reflected in Demerara Rise sediment geochemistry (ODP Leg 207): Palaeogeography, Palaeoclimatology, Palaeoecology, v. 273, p. 302–328.

Jarvis, I., Gale, A.S., Jenkyns, H.C., and Pearce, M.A., 2006, Secular variation in Late Cretaceous carbon isotopes: A new delta $\delta^{13}C$ carbonate reference curve for the Cenomanian-Campanian (99.6-70.6 Ma): Geological Magazine, v. 143, p. 561–608.

Nunez-Betelu, L.K., 1993, Rock-eval/TOC pyrolysis data from the Kanguk Formation (Upper Cretaceous), Axel Heiberg and Ellesmere islands, Canadian Arctic, Geological Survey of Canada, Open File, Volume 2727, Geological Survey of Canada.

Nunez-Betelu, L.K., 1994, Sequence stratigraphy of a coastal offshore transition, Upper Cretaceous Kanguk Formation: A palynological, sedimentological, and rock-eval characterization of a depositional sequence, Northeastern Sverdrup Basin, Canadian Arctic [Ph.D. thesis]: Calgary, Alberta, University of Calgary, 569 p.

Owens, J.D., Lyons, T.W., Li, X., Macleod, K.G., Gordon, G., Kuypers, M.M.M., Anbar, A., Kuhnt, W., and Severmann, S., 2012, Iron isotope and trace metal records of iron cycling in the proto-North Atlantic during the Cenomanian-Turonian oceanic anoxic event (OAE-2): Paleoceanography, v. 27, PA3223, doi:10.1029/2012pa002328.

Parsons, M., 1994, Geochemistry and Petrogenesis of Late Cretaceous Bentonites from the Kanguk Formation, Axel Heiberg and Ellesmere Islands, Canadian High Arctic [B.Sc. thesis]: Halifax, Dalhousie University, 131 p.

Patchett, P.J., Embry, A.F., Ross, G., Beauchamp, B., Harrison, J.C., Mayr, U., Isachsen, C.E., Rosenberg, E.J., and Spence, G.O., 2004, Sedimentary Cover of the Canadian Shield through Mesozoic Time Reflected by Nd Isotopic and Geochemical Results for the Sverdrup Basin, Arctic Canada: The Journal of Geology, v. 112, p. 39–57.

Poulton, S.W., and Canfield, D.E., 2005, Development of a sequential extraction procedure for iron: Implications for iron partitioning in continentally derived particulates: Chemical Geology, v. 214, p. 209–221.

Raiswell, R., and Canfield, D.E., 2012, The Iron Biogeochemical Cycle Past and Present, *in* Benning, L.G., ed., Volume 1: Geochemical Perspectives, European Association of Geochemistry.

Schröder-Adams, C.J., Herrle, J.O., Embry, A.F., Haggart, J.W., Galloway, J.M., Pugh, A.T., and Harwood, D.M., 2014, Aptian to Santonian foraminiferal biostratigraphy and paleoenvironmental change in the Sverdrup Basin as revealed at Glacier Fiord, Axel Heiberg Island, Canadian Arctic Archipelago: Palaeogeography, Palaeoclimatology, Palaeoecology, doi:10.1016/j.palaeo.2014.03.010. (in press).

Taylor, S.R., and McLennan, S.M., 1995, The geochemical evolution of the continental crust: Reviews of Geophysics, v. 33, p. 241–265.

van de Schootbrugge, B., Bachan, A., Suan, G., Richoz, S., and Payne, J.L., 2013, Microbes, mud and methane: Cause and consequence of recurrent Early Jurassic anoxia following the end-Triassic mass extinction: Palaeontology, v. 56, p. 685–709.

Wedepohl, K.H., 1971, Environmental influences on the chemical composition of shales and clays: Physics and Chemistry of The Earth, v. 8, p. 305–333.

Winchester, J.A., and Floyd, P.A., 1977, Geochemical discrimination of different magma series and their differentiation products using immobile elements: Chemical Geology, v. 20, p. 325–343.

Wray, D.S., and Wood, C.J., 1998, Distinction between detrital and volcanogenic clay-rich beds in Turonian–Coniacian chalks of eastern England: Proceedings of the Yorkshire Geological and Polytechnic Society, v. 52, p. 95–105.